

A Low-Cost Millimeter-Wave 5G V2X Multi-Beam Dual-Polarized Windshield Antenna

ABDELHAMID M. H. NASR^{ID} (Graduate Student Member, IEEE),
AND KAMAL SARABANDI^{ID} (Life Fellow, IEEE)

Department of Electrical and Computer Engineering, University of Michigan at Ann Arbor, Ann Arbor, MI 48105, USA

CORRESPONDING AUTHOR: A. M. H. NASR (e-mail: amhnasr@umich.edu)

This work was supported by the Verizon, Technology Development Organization.

ABSTRACT Design procedure and experimental validation for a millimeter-wave (MMW) vehicular antenna with simultaneous multi-beam, for 5G V2X application, is presented. The design overcomes the constraint for requiring both wide angular coverage and high gain through a compact multi-array design. Each array is designed to have a fixed beam direction and sufficient beamwidth so that the overall pattern guarantees simultaneous coverage in the elevation plane. The multi-array idea is a cost-effective technique compared to employing phase shifters and beam steering of a single array and avoids latency associated with beam steering. The proposed design is composed of three compact dual polarized patch arrays. Each array covers different elevation angles, and their beam maxima are chosen to be at 10° , -20° and -40° with respect to the normal of the windshield. The antenna covers the entire 28 GHz 5G band which ranges from 26.5 GHz to 29.5 GHz. Each feeding network is designed to minimize beam scanning with frequency. Dual-polarized antenna arrays are implemented to provide polarization diversity. Antenna mounting behind the laminated windshield have been investigated and proven to have a negligible effect on the antenna matching and a minor effect on the radiation pattern.

INDEX TERMS Antenna arrays, millimeter wave antenna, multi-beam antenna, vehicle-to-everything communication, and 5G antenna.

I. INTRODUCTION

THE NEED for high data rate communication for on-the-move applications is rapidly increasing. Also, improving road safety calls for high data rate vehicular communication which can facilitate autonomous driving. Dedicated Short Range Communication (DSRC) was developed as one of the first Vehicle-to-Vehicle (V2V) and Vehicle-to-Infrastructure (V2I) communication standards. Although, DSRC was proven to be viable and mature standard, it suffered from large scale deployment and relatively high latency due to the limited operating bandwidth around 5.9 GHz. Cellular Vehicle-to-Everything (C-V2X) communication showed a promising solution due to the advantages of readily available infrastructure and high data rates especially that of millimeter wave (MMW) bands. High data rate provided by MMW bands of 5G communication is a key enabler in different applications such as Vehicle-to-Everything (V2X) communication and autonomous driving [1].

High free-space path-loss in the MMW frequency range mandates employing high gain antennas, such as antenna arrays, but that results in a narrow antenna beam. The inherent frequent change of path and direction of vehicles in motion increases the rate of change of narrow beam misalignment between the vehicle and different communication nodes. A number of beam alignment algorithms have been investigated to minimize the latency associated with beam alignments. These include the use of out of band information [2] or machine learning algorithms [3].

Another solution for the beam misalignment problem is using antennas with simultaneous multiple beams [4]. Various multi-beam techniques are reported in the literature, and they can be divided into lens antennas [5], [6], [7] and planar antennas [8], [9], [10], [11], [12], [13], [14], [15]. Lens antennas achieve multibeam functionality through placement of an array of individual antennas in the focal plane of a dielectric or metasurface lens. Despite the

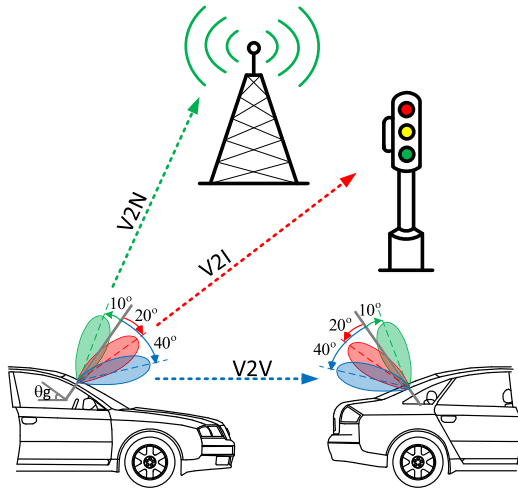


FIGURE 1. Windshield antenna beams and their different communication scenarios.

high gain that can be achieved from such antennas, their angular coverage is rather limited and they are structurally bulky which complicates their integration with vehicles. Planar multibeam antennas can be realized with various beamforming feeding structures such as: Rotman lens [8], [9] and Butler matrices [10], [11], [12], [13], [14], [15]. Planar Rotman lens structures are incorporated in beamforming due to their wide scanning capability, but they are quite lossy at millimeter-wave frequencies and occupy a very large surface area. Alternatively, arrays with Butler matrix feeding structure can be used as they are simple to design and have a simple structure that depends only on hybrid couplers, power dividers and crossovers [10]. Rescaling a conventional 4×4 Butler matrix [10] requires numerous modifications to excite different number of elements such as 3×3 matrix in [15] or 4×8 matrix in [11]. Major drawback of Rotman lens and Butler matrix is that they can only feed one polarization of the array. In other words, they are only appropriate for single-polarized elements as demonstrated in [10], [12]. To achieve dual polarization, two separate Rotman lenses or Butler matrices have to be employed for each polarization either by adding one more substrate layer [13], [14] which increases the fabrication complexity or by adding another beamforming network on the same layer which doubles the area [15]. Aside from the shortcoming of Butler matrices in regard to the dual polarization requirement, Butler matrix beamformers perform poorly for the application at hand due to high loss and need for large area which is not suitable for integration with vehicles.

Figure 1 shows different communication scenarios from the vehicle point of view such as Vehicle-to-Network (V2N), Vehicle-to-Infrastructure (V2I) and Vehicle-to-Vehicle (V2V) which requires simultaneous communication ability at different angles. In this paper, a multi-beam dual-polarized antenna array is presented to overcome the complications of alignment, maintain communication link for a moving vehicle, and guarantee simultaneous coverage for different angles

without adding latency. The antenna is composed of three dual-polarized arrays which are designed with separate feeding networks. Unlike conventional beamforming networks, series power dividers minimize the losses and the area of the antenna and hence, minimize the covered portion of the windshield. The beams are designed to cover the 90° elevation angles in the front and/or rear of vehicles with a wide azimuthal coverage for each beam. This paper presents the detailed design procedure of the antenna system that was briefly presented in [16]. Detailed analysis of the feeding network and the antenna architecture are presented and fabrication challenges of the antenna are discussed. Experimental results of the antenna by itself and the antenna mounted behind a laminated windshield are provided using far-field measurements.

This paper is organized as follows: The design procedure of the windshield antenna and the feeding network are discussed in Section II. Simulation results for individual arrays are presented in Section III. Experimental verification using far-field measurements are included in Section IV. Finally, Section V provides the summary the paper.

II. ANTENNA PLACEMENT AND SELECTION

In order to improve the chances of establishing the line-of-sight communication between a 5G MMW antenna on vehicles and another communication node, the antenna must be placed on or near the roof. Considering significant MMW propagation loss through accumulated snow and other weather-related effects, placement of 5G MMW antenna on vehicle windshield seems most suitable. Other advantages of mounting the antenna inside vehicles include: 1) temperature-controlled environment for better performance of electronics components, and 2) ease of data transfer between the 5G transceiver and the central radio unit. To avoid interfering with the driver's view, the antenna is recommended to be mounted at the top center of the windshield behind the rear-view mirror.

Antennas with directional radiation pattern must be chosen to minimize the back radiation inside the cabin and avoid gain loss. Patch antenna elements are suitable for this application as they can provide dual polarization operation easily. Polarization diversity is needed to avoid polarization mismatch due to the inherent mobility of vehicles with respect to other communication nodes such as a pedestrian or an infrastructure and the possibility of needing to establish connection through multi-path may cause polarization loss. Also as mentioned earlier, a multiple-array configuration is needed to provide both high gain and angular coverage.

A. ANTENNA DESIGN PROCEDURE

The design procedure starts with determining the antenna element. First, a dual-polarized square patch antenna is chosen as the array element due to its ease of fabrication, high front-to-back radiation ratio, and dual-polarization operation. Dual polarization can be achieved either through proximity

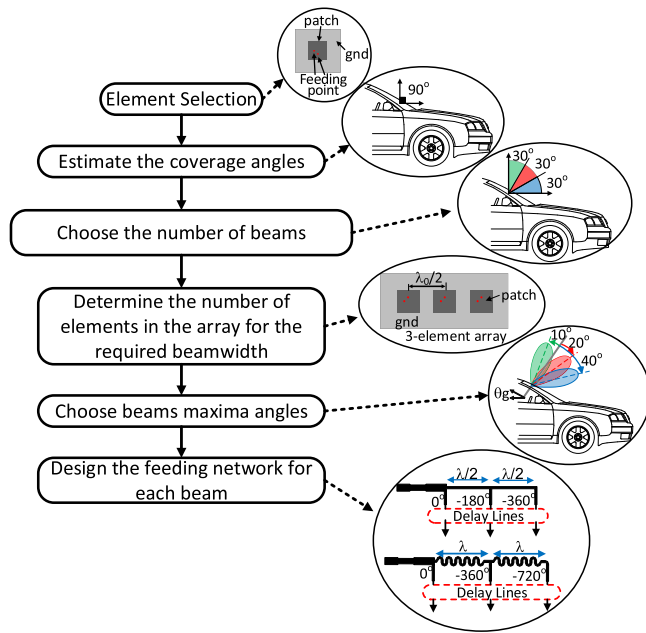


FIGURE 2. Design procedure chart.

feeding [17] or probe feeding of each element. Probe feeding is utilized to allow more flexible control over the beam angle. The next step is determination of the beams' maxima in accordance with windshield inclination angle. Most of vehicles' windshields have an inclination angle with horizon of about 30° or more and that needs to be accounted for in the design of the antenna beam direction [18].

In order to cover the 90° elevation angles, and maintain a maximum gain of about 10 dB, three simultaneous beams are required. In this case the minimum beam width for each beam should be around 30° . To determine the number of elements in each array, arrays with different number of patch elements with $\lambda_0/2$ spacing are simulated and it was found that the minimum 30° beam width can be achieved using at least three elements. Therefore, the required antenna should be composed of three arrays, with each array having three elements. Considering the windshield inclination angle, the beams' maxima for the arrays are to be at 10° , -20° and -40° with respect to the windshield normal as shown in Fig. 1. The next step pertains to the design of the feeding network for each sub-array. This is done using a three-way series power divider which is simply composed of either $\lambda/2$ or λ series sections between the outputs of the divider as shown in the inset of Fig. 2. The choice between a $\lambda/2$ or a λ series section is determined based on the space constraints and the required bandwidth of the array. Phase delay lines are then added to each output of the divider to provide the required phase progression for each beam tilt angle. The power divider lines, and the phase delay lines are then tuned to minimize the frequency beam scanning. The design of the feeding network is repeated for each beam and polarization. Finally, all the arrays are then assembled together on the same PCB and a final tuning to overcome the issues related

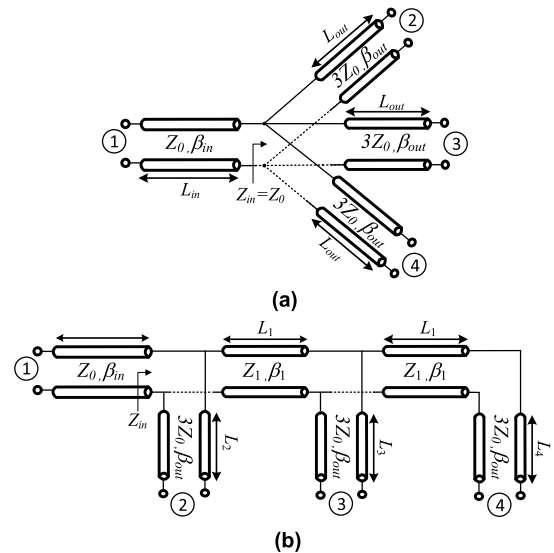


FIGURE 3. (a) Conventional three-way transmission line power divider and (b) Series three-way power divider with $L_1 = n\lambda/2$ sections.

to mutual coupling between the arrays is considered. The design procedure flowchart is depicted in Fig. 2.

B. FEEDING NETWORK DESIGN

The feeding network is designed based on the conventional transmission line impedance power divider shown in Fig. 3(a). An equal three-way power division is achieved through equal impedance ratios between each output transmission line and the input transmission line. To minimize the area of the feeding network, a conventional transmission line power divider can be converted to a series power divider through inserting transmission line sections with lengths $L_1 = n\lambda/2$ between output ports as depicted in Fig. 3(b). In order to simplify the analysis of the series power divider, the characteristic impedance of the inserted section is set to be equal to output port impedances ($Z_1 = 3Z_0$). Considering very short output transmission lines ($L_2 = L_3 = L_4 \approx 0$), the scattering parameters of the divider are evaluated to be as follows:

$$S_{11} = \frac{j \tan \theta}{2 + j3 \tan \theta} \quad (1)$$

$$S_{21} = \frac{1}{\sqrt{3}} \frac{2 + j4 \tan \theta}{2 + j3 \tan \theta} \quad (2)$$

$$S_{31} = \frac{e^{-j\theta}}{\sqrt{3}} \frac{2 + j2 \tan \theta}{2 + j3 \tan \theta} \quad (3)$$

$$S_{41} = \frac{e^{-j2\theta}}{\sqrt{3}} \frac{2 + j2 \tan \theta}{2 + j3 \tan \theta} \quad (4)$$

where θ is the inserted transmission line phase delay ($\theta = \beta_1 L_1$).

Unlike the conventional power divider which provides in-phase frequency-independent power division, the series power divider scattering parameters shows a frequency-dependent phase difference between its outputs and the phase

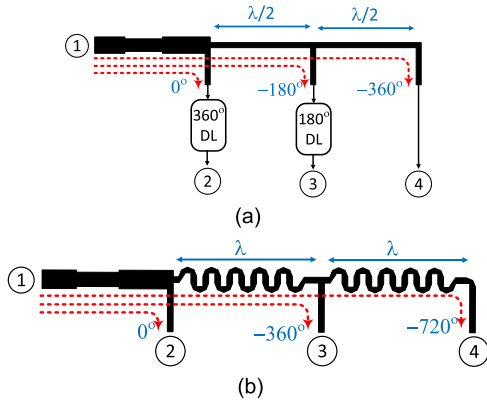


FIGURE 4. In phase three-way equal power divider with (a) $\lambda/2$ sections and (b) λ section.

difference value at the operating frequency depends on the value of n . For even values of n ($\theta_0 = 2n\pi$), the outputs are in-phase, while for odd values of n ($\theta_0 = \pi \pm 2n\pi$), the outputs are 180° out of phase.

Consequently, a three-way in-phase series power divider with $\lambda/2$ sections ($\lambda/2$ -divider) can be achieved by adding a 360° delay line to port 2 ($\beta_{out}L_2 = 2\pi$), and a 180° delay line is added to port 3 ($\beta_{out}L_3 = \pi$) as depicted in Fig. 4(a).

The analysis of the series divider can be used to compare the two used topologies, $\lambda/2$ -divider shown in Fig. 4(a) and λ -divider in Fig. 4(b). The fractional bandwidth of the magnitude of the s-parameters can be calculated from the magnitude of the ratio ($S_{X1}(\theta)/S_{X1}(\theta_0)$). The magnitude bandwidth is limited by transmission to port 3 or port 4 (as they have the same magnitude expression) and expressed as follows:

$$BW_f = \frac{2\Delta\theta}{\theta_0} \Big|_{S_{31}} = \frac{2}{\theta_0} \tan^{-1} \sqrt{\frac{4(1 - |S_{31}(\theta)/S_{31}(\theta_0)|^2)}{(9|S_{31}(\theta)/S_{31}(\theta_0)|^2 - 4)}} \quad (5)$$

where θ_0 is the phase delay of the inserted transmission lines at the operating frequency. This indicates that the magnitude fractional bandwidth of the λ -divider is half of that of the $\lambda/2$ -divider for the same ($S_{31}(\theta)/S_{31}(\theta_0)$) ratio. It is worth mentioning that both dividers satisfy the required bandwidth (26.5 GHz to 29.5 GHz) for ($S_{31}(\theta)/S_{31}(\theta_0)$) ratio of 1.5 dB.

To examine the frequency beam scanning behavior of the array, the rate of change of phase difference between the output ports versus frequency must be examined. This can be calculated by computing the slope of the phase difference (ψ) with respect to frequency. However, to come up with a dimensionless quantity we compute the derivative of ψ with respect to the phase delay ($\theta = \beta_1 L_1$) with is linearly proportional to frequency. The rate of change of phase difference with respect to delay (frequency) is calculated for both dividers. The value of the rate of change of the $\lambda/2$ -divider calculated between ports 4 and 2 ($\psi_{42} = \angle S_{41} - \angle S_{22}$) which

is given by:

$$\frac{\partial \psi_{42}}{\partial \theta} \Big|_{\lambda/2\text{-divider}} = \frac{1 + \tan^2 \theta}{(2\tan^2 \theta + 1)^2 + \tan^2 \theta} \approx \frac{1}{1 + 4\Delta\theta} \Big|_{\theta = \theta_0 + \Delta\theta} \quad (6)$$

$\Delta\theta \ll 1$

This equation shows that rate of change of phase difference with respect to delay is less than one and decreases with increasing $\Delta\theta$. On the other hand, the rate of change of phase difference with respect to delay for the λ -divider between ports 4 and 2 is given by:

$$\frac{\partial \psi_{42}}{\partial \theta} \Big|_{\lambda\text{-divider}} = -3 \frac{1 + 2\tan^2 \theta}{1 + 4\tan^2 \theta} \approx -3 \Big|_{\theta = \theta_0 + \Delta\theta} \quad (7)$$

$\Delta\theta \ll 1$

This shows rate of change of phase difference with respect to delay for the λ -divider is at least three times higher than that for the $\lambda/2$ -divider. For arrays with tilt angles 10° and 20° , the $\lambda/2$ -divider is used and thus have a lower beam scanning with frequency. For the array with tilt angle 40° , λ -divider has to be used because of space limitation.

The total loss values are comparable for both dividers, however, the $\lambda/2$ -divider loss are equal for each port, whereas for the λ -divider case, the loss in port 4 path is higher than that in port 2 path. Changing the delay lines lengths for a different tilt angle other than zero increases the loss in the λ -divider but tends to equalize the loss for each port. On the other hand, changing the delay lines in the $\lambda/2$ -divider make their lengths shorter and thus the total loss is reduced but it makes the port outputs unequal.

The desired beams maxima for the antenna system are 10° , -20° and -40° and according to the simulations of a uniform three-element array of patches with $\lambda_0/2$ spacing, the phase differences between the divider outputs should be -37° , 69° and 132° , respectively. For the 10° and -20° beams, a $\lambda/2$ -divider is incorporated. For the 40° beam angle, the delay lines for the $\lambda/2$ -divider become very short which complicates the achievable output phases for the given array spacing and divider dimensions. Therefore, as mentioned before a λ -divider is used as its dimensions allow more flexibility to control the phase for each output. The lengths of the output delay lines are chosen to maximize the power division uniformity among the elements. This provides forward tilted beams for the 10° and 20° beams pointing away from the input feed connector and a backward beam for the 40° beam pointing towards the input feed connector.

III. SIMULATION RESULTS

Each antenna array is designed separately, and the feeding networks are adjusted to minimize beam scanning with frequency. The arrays are designed using two substrates. The lower layer is RT/duroid 5880 substrate, a 0.254 mm thick substrate for the feeding network, and the top layer is a 0.504 mm thick substrate for the antenna with 18 oz copper thickness. Each array is designed for a dual-polarized operation, the vertical polarization corresponds to y-direction and horizontal polarization corresponds to the x-direction as depicted in Fig. 5.

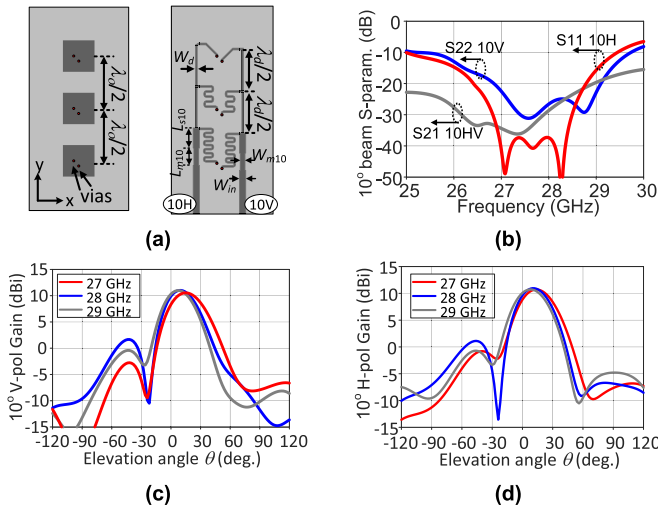


FIGURE 5. 10° beam array design. (a) layout of the top and bottom layers. (b) Scattering parameters of the V-pol and H-pol ports. (c) V-pol and (d) H-pol elevation radiation patterns at 27, 28 and 29 GHz.

A. 10° BEAM ANTENNA ARRAY

Top and bottom layers of the 10° beam array are shown in Fig. 5(a). The top layer shows square patch elements with spacing set to $\lambda_0/2$. Square patches are fed from two points to feed two orthogonal polarizations. The bottom layer shows two feeding networks, one for each polarization, using $\lambda/2$ -dividers. The matching bandwidth is improved through a stepped impedance section at the input of each feeding network. The simulated 10 dB reflection coefficients bandwidth for the V-pol is 13.5% ranging from 25.9 GHz to 29.7 GHz. While the simulated H-pol bandwidth is 16% ranging from 25 GHz to 29.5 GHz as depicted in Fig. 5(b). Isolation between the two ports is better than 18 dB over the operating bandwidth. Simulated patterns along the array axis (yz-plane) for V-pol and H-pol are plotted in Fig. 5(c) and 5(d), respectively, at three different frequencies 27 GHz, 28 GHz, and 29 GHz. The V-pol beams maxima directions at 27 GHz, 28 GHz and 29 GHz are 13°, 10° and 8°, respectively, away from the input feeding connector. The simulated Gain/HPBW at these frequencies are 10.5 dBi/36°, 11 dBi/32° and 10.96 dBi/31°. Similarly, the H-pol beam maxima directions at 27, 28 and 29 GHz are 13°, 10° and 8° with Gain/HPBW of 10.7 dBi/36°, 10.9 dBi/34° and 10.7 dBi/34°.

B. 20° BEAM ANTENNA ARRAY

Top and bottom layers of the 20° beam array are shown in Fig. 6(a). The delay lines in the feeding network are shorter than the case of 10° beam as the required phase difference between the elements is larger. The simulated 10 dB reflection coefficients bandwidth for the V-pol is 13.2% ranging from 26.3 GHz to 30 GHz. While the simulated H-pol bandwidth is 11.8% ranging from 26.3 GHz to 29.6 GHz as depicted in Fig. 6(b). Isolation between

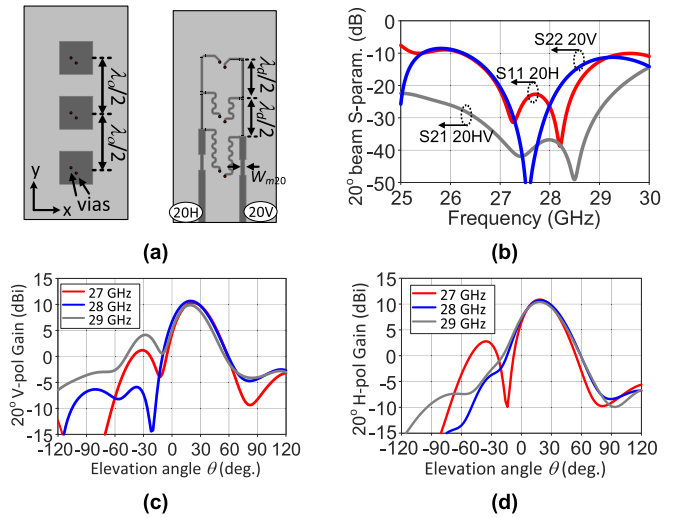


FIGURE 6. 20° beam array design. (a) Layout of the top and bottom layers. (b) Scattering parameters of the V-pol and H-pol ports. (c) V-pol and (d) H-pol elevation radiation patterns at 27, 28 and 29 GHz.

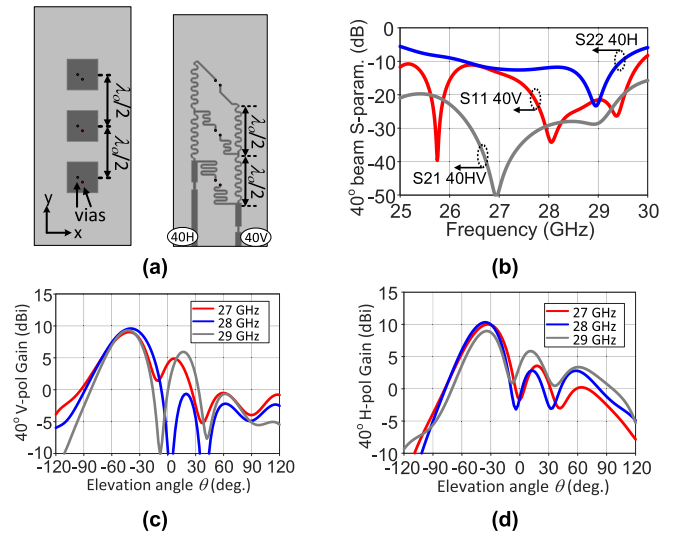


FIGURE 7. 40° beam array design. (a) Layout of the top and bottom layers. (b) Scattering parameters of the V-pol and H-pol ports. (c) V-pol and (d) H-pol elevation radiation patterns at 27, 28 and 29 GHz.

the two ports is more than 20 dB over the entire operating bandwidth. Simulated elevation patterns in the zy-plane for V-pol and H-pol arrays are plotted in Fig. 6(c) and 6(d), respectively. V-pol beam maxima directions at 27 GHz, 28 GHz and 29 GHz are at 22°, 20°, 20° from the normal (away from the input feeding connector) with Gain/HPBW of 10.3 dBi/34.8°, 10.66 dBi/36.4° and 9.85 dBi/ 33.4°. While H-pol beam maxima directions are at 18°, 20° and 18° with Gain/HPBW 10.8 dBi/ 34.5°, 10.7 dBi/37.7° and 10.4 dBi/38.4°, respectively.

C. 40° BEAM ANTENNA ARRAY

This array is designed with a λ -divider. Fig. 7(a) depicts the layout of the patch layer and the feeding network layer. For optimum matching and minimal beam scanning with

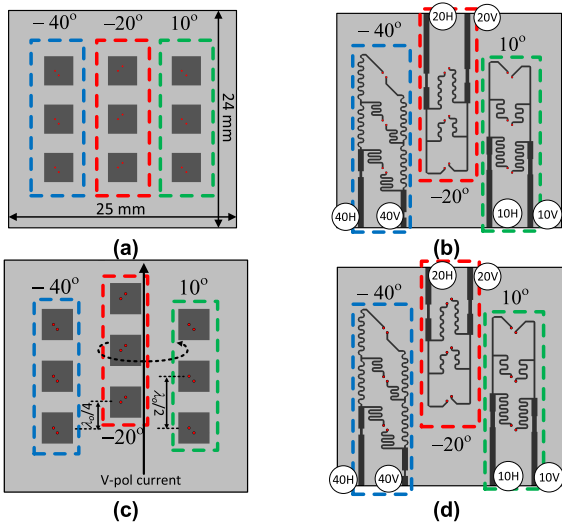


FIGURE 8. Layout of the three-beam array assembled on a single PCB. The top layer (a) and the bottom layer (b) are shown. Another arrangement with a vertically offset middle array (top layer (c) and bottom layer (d)).

frequency, the delay lines are added such that the beam points towards the input feeding connector. The simulated 10 dB reflection coefficients, shown in Fig. 7(b), have a bandwidth of 17% (ranging from 25 GHz to 29.9 GHz. While the simulated H-pol is 12.8% ranging from 25.9 GHz to 29.5 GHz) for the V-pol. Fig. 7(c) and Fig. 7(d) show the simulated V-pol and H-pol patterns, respectively. V-pol beam maxima directions at 27 GHz, 28 GHz and 29 GHz are at 42° , 40° , 42° with Gain/HPBW of 9.1 dBi/ 41° , 9.6 dBi/ 44° and 9.3 dBi/ 36° , respectively. H-pol beam maxima directions are at 40° , 38° and 42° with Gain/HPBW 10.8 dBi/ 34.5° , 10.7 dBi/ 37.7° and 10.4 dBi/ 38.4° at the aforementioned frequencies.

As the beam angle increases, the coupling between elements increases making it harder to get a wide bandwidth. Bandwidth for the H-pol beam is narrower as the magnetic fields corresponding to H-pol currents directly couple from one element to another, unlike the V-pol magnetic fields. The feeding network including the power divider and the delay lines are tuned for each polarization to minimize beam frequency scanning with frequency and provide the required reflection coefficient bandwidth. The sidelobe level (SLL) is higher than that for the 10° and 20° array, but the gain is approximately 10 dBi for all frequency and that is more important than the SLL in our application in order to satisfy the required coverage range with acceptable gain values.

D. INTEGRATION OF ARRAYS

For compactness and ease of operation, the arrays should be integrated on a common printed circuit board (PCB). To obtain the required beam angles (10° , -20° and -40°), the arrays are arranged as depicted in Fig. 8(b), such that the feeding network of the -20° is in the opposite side of other arrays.

The designed antenna system is suitable for integration with the RF communication chip directly to the antenna PCB which overcomes the high cable loss at millimeter wave frequencies. The spacing between the arrays is set to 7 mm to minimize the coupling between the array elements and the feeding lines in order to maintain more than 20 dB of isolation among all ports.

The effects of the ground plane size on the radiation patterns are co-optimized by the feed network while minimizing the ground size of the arrays to be $25 \text{ mm} \times 24 \text{ mm}$ which corresponds to $2.33\lambda \times 2.24\lambda$ at 28 GHz. Magnetic field coupling among the adjacent arrays for V-pol ports is higher than that for H-pol ports. To minimize this magnetic field coupling for the V-pol channels, the adjacent arrays are offset in the vertical direction [19]. The middle array is vertically offset to minimize the horizontal magnetic field linking between elements of adjacent arrays as shown in Fig. 8(c and d).

Even though the proposed multibeam antenna structure requires separate array apertures for each beam, unlike its counterpart that uses Butler matrix, the area of the series-fed multibeam antenna is less than half the area of 3×3 butler matrix [15]. Multibeam antennas that incorporate Butler matrices exhibit high loss and low efficiency which is not suitable for MMW applications. In contrast, the simulated efficiency of the proposed series-fed multibeam antenna is better than 93%. The total length of the series power divider is comparable to the length of the total array which allows feeding dual-polarized arrays without a huge requirement for additional surface area or complex multi-layer substrate. The proposed structure requires two substrate layers with only thru-hole vias which can be fabricated with a low-cost PCB.

IV. EXPERIMENTAL RESULTS

Although the antenna system is designed to simplify the integration with 5G chips, experimental testing of the antenna solely, requires soldering connectors to the antenna ports. Adding connectors to the array is challenging since the operating wavelength is comparable to the dimensions of the connectors. These connectors affect the radiation characteristics of the arrays. RF connectors for testing also affect the coupling level among the arrays. To minimize such effects, different array and connector arrangements are simulated and optimized. The fabricated antenna structure is shown in Fig. 9. The arrays are ordered such that 10° array is in between the -20° array and -40° array to minimize the coupling between -20° and -40° arrays. The antenna is fabricated using two Rogers RT/duroid 5880 layers, the patch layer thickness is 0.508 mm and the feeding layer is 0.254 mm thick with a copper layer in between as the ground plane. Both layers are held together using a prepreg with a 0.0845 mm thickness. A coplanar waveguide (CPW) to microstrip transition is added to each port where the ground of the CPW is connected to the middle ground layer through vias as demonstrated in the inset of

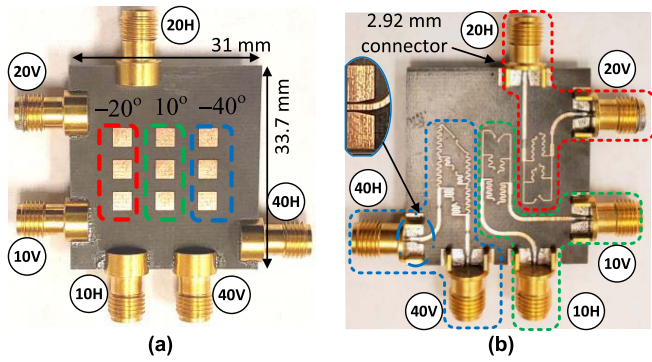


FIGURE 9. Photos of the fabricated antenna. (a) Top layer. (b) Bottom Layer.

Fig. 9(b) to allow soldering the ground plane to the connectors. 2.92 mm connectors are soldered to each port to allow characterization up to 30 GHz. The area of the antenna PCB increases to 31 mm × 33.7 mm due to the extra feeding length and transitions added to include the connectors.

Matching and isolation are characterized through measuring the scattering parameters. Radiation characteristics are evaluated through far-field antenna pattern measurements. The measured scattering parameters of 10° beam ports are shown in Fig. 10(a). Reflection coefficients of the V-pol and H-pol ports are matched over 26.5 GHz to 29.5 GHz. Coupling between V-pol and H-pol is better than 30 dB over the same band. Fig. 10(b) depicts the measured 20° beam parameters. The H-pol reflection coefficient is matched over the entire frequency range and 20° V-pol is matched from 25.82 GHz to 29.81 GHz. Coupling between H-pol and V-pol ports is better than 25 dB over the operating frequency range. The measured 40° beam scattering parameters are plotted in Fig. 10(c). The H-pol reflection coefficients' 10 dB bandwidth is 4 GHz from 25.6 GHz to 29.6 GHz. The V-pol port is matched over the operating frequency range. Coupling between H-pol and V-pol ports is better than 22 dB over the operating frequency range. Measurements and EM simulations are in an excellent agreement.

The far-field radiation patterns are characterized in an anechoic chamber with the antenna under test connected to the transmit end and a Ku-band horn connected to the receive end. The antenna under test is mounted on a foam sheet that is fixed to a turntable and a Ku-band horn antenna is connected to a spectrum analyzer on the other end as shown in Fig. 11. The setup allows far-field radiation patterns measurements for angles that ranges from -150° to 150°. Measurements were performed at 28 GHz. The far-field gain of the Ku-band horn was first characterized through transmission measurements between two identical horns and then one of them is replaced with the antenna under test. The gain of the horn antenna was calculated to be 21 dBi all over the operating frequency range of the antenna under test.

The measured far-field radiation patterns are compared to EM simulations at 28 GHz in Fig. 12. The radiation

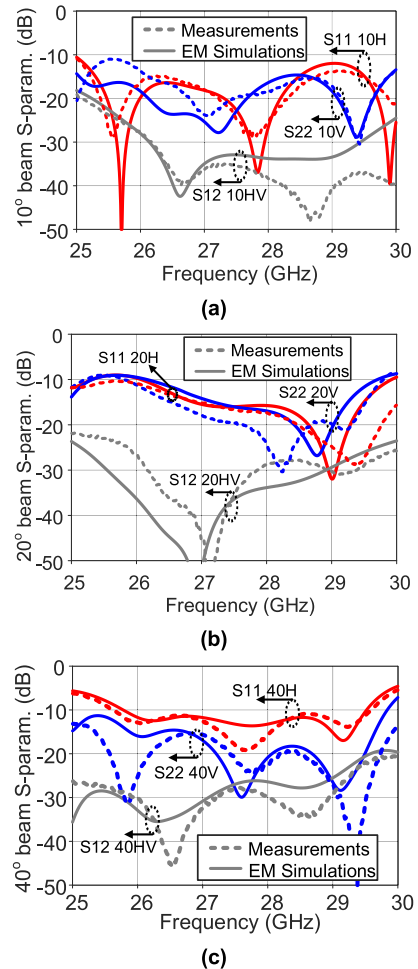


FIGURE 10. (a) S parameters for the 10° beam. (b) 20° beam. And (c) 40° beam. Reflection coefficients for H-pol ports are in red, V-pol ports in blue and isolation between V-pol and H-pol are in grey.

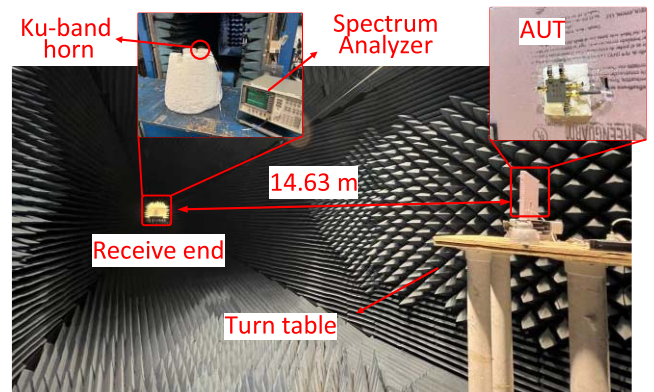


FIGURE 11. Far field measurement setup.

pattern of the 10° H-pol array in Fig. 12(a) has the peak angle/HPBW around 11° /31° compared to simulated peak angle/HPBW of 10° /36° and the peak angle varies within ±3° across the operating frequency range. The measured gain in Fig. 13(a) is 12.2 dBi compared to simulated gain of 12 dBi at 28 GHz and the gain maximum variation is

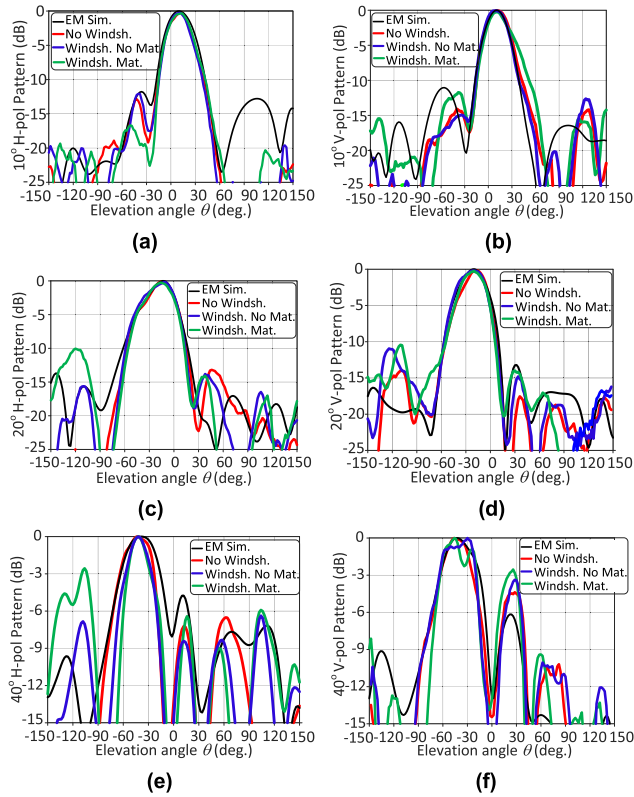


FIGURE 12. Measured far-field radiation patterns at 28 GHz. (a) 10° H-pol, (b) 10° V-pol, (c) 20° H-pol, (d) 20° V-pol, (e) 40° H-pol, (f) 40° V-pol.

TABLE 1. Measured radiation pattern parameters.

	EM sim. Peak angle/HPBW (deg.)	FF. Peak angle/HPBW (deg.)	EM sim. Gain (dBi)	FF. Gain (dBi)
10° H-pol	10°/36°	11°/31°	12	12.2
10° V-pol.	10°/29°	10°/32°	11	11.3
20° H-pol	14°/38°	16°/37°	9.9	9.7
20° V-pol	20°/38°	18°/38°	10.5	10.7
40° H-pol	38°/48°	40°/41°	9.5	9.4
40° V-pol	42°/46°	44°/40°	8.79	8.3

Gain values are calculated at 28 GHz.

1.32 dB within the operating frequency range. Fig. 12 (b) shows the radiation pattern of the 10° V-pol array. The radiation peak angle/HPBW is measured to be 10°/32° compared to 10°/29° simulated values. The measured gain is 11.3 dBi compared to 11 dBi simulated value and it varies within 1.47 dB over the desired frequency range as shown in Fig. 13(b).

Fig. 12 (c) and Fig. 12 (d) depict the radiation patterns for the 20° H-pol array and 20° V-pol array, respectively. The angle of maximum radiation/ HPBW of the 20° H-pol is 16° /37° while the gain at the center frequency is 10.7 dBi compared to the simulated 10.5 dBi and it varies 2.6 dB within the operating range. Similarly, the angle of

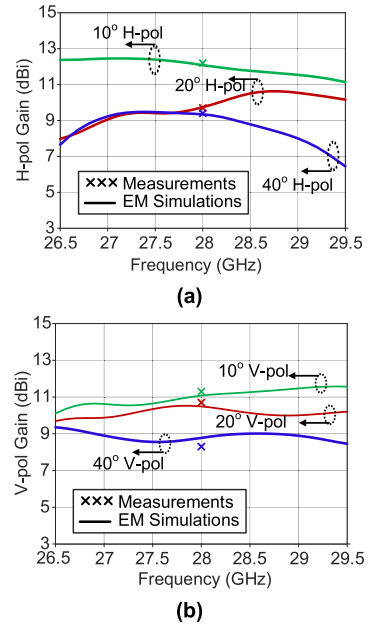


FIGURE 13. Far field gain for (a) H-pol ports and (b) V-pol ports.

maximum radiation/ HPBW of the 20° V-pol is 18° /38° with the gain at the center frequency is 10.7 dBi compared to the simulated 10.5 dBi and it varies 0.9 dB within the operating range.

The radiation patterns for the 40° H-pol array and 40° V-pol array are presented in Fig. 12(d) and Fig 12(e), respectively. The angle of maximum radiation/ HPBW of the 40° H-pol is 40° /41° while the gain at the center frequency is 9.4 dBi and it varies within 2.7 dB within the operating range. On the other hand, the angle of maximum radiation/ HPBW of the 40° V-pol is 44° /40° with the gain at the center frequency is 8.3 dBi and it varies 0.8 dB within the operating range. The measured radiation pattern and gain are in a very good agreement with the simulated ones. The discrepancy between measurements and simulations can be attributed to uncertainties in the parameters of the prepreg used as the adhesion layer between RT/duroid 5880 layers and other fabrication tolerances and the imperfections in the measurement’s setup. The measured cross-polarized radiation of all the beams is 24 dB lower than the co-polarized radiation along the array direction of maximum radiation.

The measured 40° beam patterns show more discrepancy than other beams compared to simulations due to higher connector coupling for the most tilted beam. This issue is demonstrated by performing a near-field measurements only above the patches to exclude the connectors and cables effects. The near-field data of the antennas are collected using a non-intrusive electro-optical field measurement system (NeoScan) [20]. Since, the system utilizes a very small non-metallic probe the interaction between the probe and the radiating elements is minimized. This also simplifies transformation of the measured near-field data to far-field patterns. A 3D-printed jig is fabricated to hold the

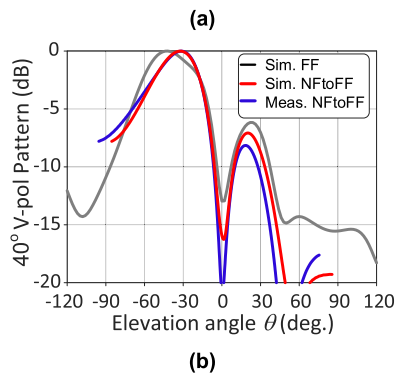
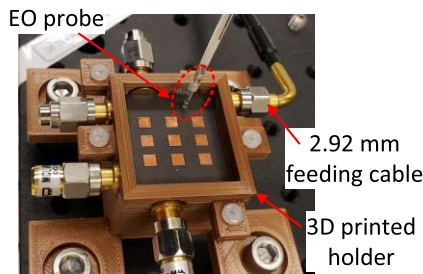


FIGURE 14. Effect of the connector on the radiation pattern. (a) Near measurements setup. (b) Normalized radiation patterns for 40° V-pol port.

antenna flat and provide mechanical support for the connects as shown in Fig. 14(a). The probe is set at a 2 mm height above the surface of the antenna for maximum field sensitivity and the scanned area is set to 20 mm × 20 mm within the borders of the 3D-printed jig with 0.2 mm step size. Each port is connected to a 28 GHz source with 20 dBm output power. The near-fields corresponding to a similar area is extracted from the EM simulations and then the far field patterns are calculated from the near-field data and plotted in Fig. 14(b). EM simulations and measurements of the calculated far-fields from near fields within the connectors' boundary are in an excellent agreement. However, the simulated far-fields including the connector shows a slightly different radiation pattern with a wider main lobe which indicates that the discrepancy between measured far-fields and simulated far-fields are due to connector coupling. This will not be an issue when RF chips are integrated with the antenna system.

V. WINDSHIELD EFFECT ON THE ANTENNA

The commonly used windshield is made of laminated glass, which is composed of a thin PVB (0.76 mm) layer sandwiched between two glass layers with similar thickness of 2.1 mm as shown in Fig. 15(a). The laminated structure is essential to prevent shattering of the windshield upon an accident. The glass dielectric constant is found to be 6.48 and the loss tangent of 0.024 at 30 GHz as shown in [21]. While, the PVB has a dielectric constant of 2.5 as reported in the literature [22]. The reflection coefficients of an incident plane wave on different glass stacks are shown in Fig. 16 as

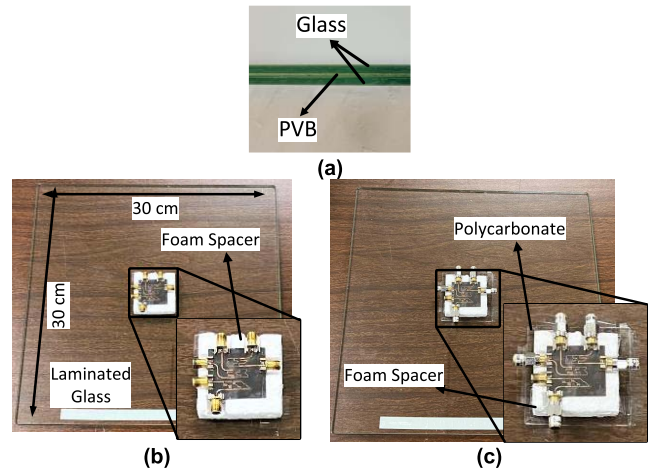


FIGURE 15. (a) Laminated windshield stack. (b) AUT attached to the windshield via a foam spacer. (c) Polycarbonate used as a matching layer to the windshield.

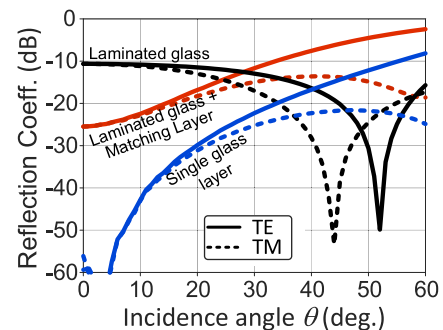


FIGURE 16. Unit cell simulation of different glass stacks at 28 GHz.

a function of the incident angle. The plane wave simulations were performed using periodic boundary conditions of a 3 mm × 3 mm unit cell. Although, the plane wave reflection coefficient does not accurately represent the effect of the windshield, it provides an intuition about the interaction of the waves emitted from the arrays with the windshield. A single glass layer has a thickness that corresponds to $\lambda/2$ at 28 GHz and this guarantees an optimum transmission through the glass for a normal incident plane wave as shown in Fig. 16. A laminated glass, however, has a higher reflection coefficient at the normal incidence, but the reflection decreases at higher incidence angles. Note that the maximum reflection coefficient value is below -10 dB for all incidence angles. In an attempt to improve the matching at normal incidence, an additional layer of transparent polycarbonate with a thickness of 2.5 mm and dielectric constant of 2.54 is added to the stack. This stack shows an improved matching at normal incidence, but it exhibits a degraded performance for angles higher than 30°.

The effect on the windshield is tested by attaching the antenna directly to a 12" × 12" windshield sample as shown in Fig. 15(b) and by attaching the antenna to a matching layer which is fixed to the windshield as depicted in Fig. 15(c). A 5 mm thick foam spacer is incorporated to hold

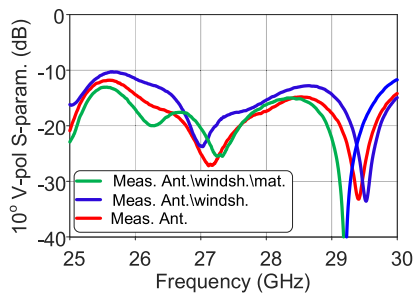


FIGURE 17. Effect of the windshield on the antenna reflection coefficient.

the antenna away from the windshield surface, as shown in Fig. 15(b) and 15(c), to cope with the connector dimensions.

Figure 17 depicts the matching of the 10° V-pol port with and without polycarbonate matching layer which shows that the windshield has a minor effect on the reflection coefficient. All other ports exhibit similar behavior with all ports being matched while the antenna is attached to the windshield. The spacing between the antenna and the windshield does not have a significant effect on the matching and the connectors dimensions restrict the minimum spacing value.

The radiation patterns of the antenna with the windshield are included in Fig. 12. The normalized radiation patterns for 10° beams are very close to that of the antenna without the windshield in terms of the beamwidth and beam maximum angle. While the 20° H-pol beam shows a higher side lobe level if a matching layer is used (as expected from Fig. 16). In the case of 40° beams, the main lobe is close to the case without the windshield with some fluctuations in the pattern, while the side lobes are higher especially for the case with the matching layer case.

The changes in the radiation pattern can be attributed to the coupling of the antenna with the connectors. The losses in the glass and the PVB cause some reduction in the gain values. The peak gain of the 10° H-pol and 10° V-pol are reduced by 0.67 dB and 0.5 dB, respectively. While, the peak gain of 20° H-pol and 20° V-pol are decreased by 1.1 dB and 0.85 dB. Finally, the peak gain of 40° H-pol and 40° V-pol are lowered by 1.2 dB and 1.4 dB, respectively.

VI. CONCLUSION

A multi-beam dual-polarized vehicular 5G antenna array system is proposed for V2X communication. The antenna is designed for windshield mounting and it has a small size that minimizes the blockage of the driver's field of view. The simultaneous multi-beam antenna provides a relatively high gain and angular coverage in the elevation plane. This MMW 5G antenna is composed of three separate dual polarized arrays each providing a beam to cover at least a 30° beamwidth angle in the elevation plane and a wide beam coverage in the azimuth plane. The three beams' maxima are designed to be at 10° , -20° and -40° with respect to the normal direction of the windshield. A connectorized version of the antenna is fabricated for validation. All the antenna ports are matched over the 5G 28 GHz band that

covers 26.5 GHz to 29.5 GHz. The radiation characteristics are evaluated using far-field measurements and they are in a very good agreement with the EM simulations. The effects of the windshield have been characterized and the windshield introduces a minor effect on the radiation characteristics without the need for a matching layer.

ACKNOWLEDGMENT

The NeoScan system used in the measurements is commercialized by EMAG Technologies in which Prof. K. Sarabandi is a principal.

REFERENCES

- [1] J. Choi, V. Va, N. Gonzalez-Prelcic, R. Daniels, C. R. Bhat, and R. W. Heath, "Millimeter-wave vehicular communication to support massive automotive sensing," *IEEE Commun. Mag.*, vol. 54, no. 12, pp. 160–167, Dec. 2016.
- [2] N. González-Prelcic, A. Ali, V. Va, and R. W. Heath, "Millimeter-wave communication with out-of-band information," *IEEE Commun. Mag.*, vol. 55, no. 12, pp. 140–146, Dec. 2017.
- [3] Y. Wang, A. Klautau, M. Ribero, A. C. K. Soong, and R. W. Heath, "MmWave vehicular beam selection with situational awareness using machine learning," *IEEE Access*, vol. 7, pp. 87479–87493, 2019.
- [4] W. Hong et al., "Multibeam antenna technologies for 5G wireless communications," *IEEE Trans. Antennas Propag.*, vol. 65, no. 12, pp. 6231–6249, Dec. 2017.
- [5] T. P. Nguyen, C. Pichot, C. Migliaccio, and W. Menzel, "Study of folded reflector multibeam antenna with dielectric rods as primary source," *IEEE Antennas Propag. Lett.*, vol. 8, pp. 786–789, 2009.
- [6] M. Jiang, Z. N. Chen, Y. Zhang, W. Hong, and X. Xuan, "Metamaterial-based thin planar lens antenna for spatial beamforming and multibeam massive MIMO," *IEEE Trans. Antennas Propag.*, vol. 65, no. 2, pp. 464–472, Feb. 2017.
- [7] G. Liu, M. R. D. Kodnoeih, T. K. Pham, E. M. Cruz, D. González-Ovejero, and R. Sauleau, "A millimeter-wave multibeam transparent transmitarray antenna at Ka-band," *IEEE Antennas Wireless Propag. Lett.*, vol. 18, no. 4, pp. 631–635, Apr. 2019.
- [8] K. Tekkoku, M. Ettorre, L. Le Coq, and R. Sauleau, "Multibeam SIW slotted waveguide antenna system fed by a compact dual-layer Rotman lens," *IEEE Trans. Antennas Propag.*, vol. 64, no. 2, pp. 504–514, Feb. 2016.
- [9] Y. J. Cheng et al., "Substrate integrated waveguide (SIW) Rotman lens and its Ka-band multibeam array antenna applications," *IEEE Trans. Antennas Propag.*, vol. 56, no. 8, pp. 2504–2513, Aug. 2008.
- [10] H. Chu, Y.-X. Guo, and Z. Wang, "60-GHz LTCC wideband vertical off center dipole antenna and arrays," *IEEE Trans. Antennas Propag.*, vol. 61, no. 1, pp. 153–161, Jan. 2013.
- [11] Y. Cao, K.-S. Chin, W. Che, W. Yang, and E. S. Li, "A compact 38 GHz multibeam antenna array with multifolded butler matrix for 5G applications," *IEEE Antennas Wireless Propag. Lett.*, vol. 16, pp. 2996–2999, 2017.
- [12] Y. J. Chen, W. Hong, and K. Wu, "Millimeter-wave multibeam antenna based on eight-port hybrid," *IEEE Microw. Wireless Compon. Lett.*, vol. 19, no. 4, pp. 212–214, Apr. 2009.
- [13] Y. Li, J. Wang, and K.-M. Luk, "Millimeter-wave multibeam aperture-coupled magnetolectric dipole array with planar substrate integrated beamforming network for 5G applications," *IEEE Trans. Antennas Propag.*, vol. 65, no. 12, pp. 6422–6431, Dec. 2017.
- [14] Y. Li and K.-M. Luk, "60-GHz dual-polarized two-dimensional switch beam wideband antenna array of aperture-coupled magneto-electric dipoles," *IEEE Trans. Antennas Propag.*, vol. 64, no. 2, pp. 554–563, Feb. 2016.
- [15] R. Gong, Y. Ban, J. Lian, Y. Liu, and Z. Nie, "Circularly polarized multibeam antenna array of ME dipole fed by 5×6 butler matrix," *IEEE Antennas Wireless Propag. Lett.*, vol. 18, no. 4, pp. 712–716, Apr. 2019.
- [16] A. Nasr, K. Sarabandi, and M. Takla, "Multi-beam dual-polarized windshield antenna with wide elevation coverage for 5G V2X applications," in *Proc. IEEE APSURSI*, 2020, pp. 1333–1334.

- [17] C. Deng, B. Yektakhah, and K. Sarabandi, "Series-fed dual-polarized single-layer linear patch array with high polarization purity," *IEEE Antennas Wireless Propag. Lett.*, vol. 18, no. 9, pp. 1746–1750, Sep. 2019.
- [18] G. Walsh and E. I. Pearce, "The influence of automobile wind-screen rake on effective light transmittance," *Ophthalmic Physiol. Opt.*, vol. 30, no. 6, pp. 785–789, 2010.
- [19] A. Abbaspour-Tamijani and K. Sarabandi, "An affordable millimeter-wave beam-steerable antenna using interleaved planar sub arrays," *IEEE Trans. Antennas Propag.*, vol. 51, no. 9, pp. 2193–2202, Sep. 2003.
- [20] "NeoScan System. EMAG Technologies Inc." Accessed: Mar. 16, 2022. [Online]. Available: <https://emagtech.com/neoscan-system/>
- [21] A. M. H. Nasr, A. Y. Nashashibi and K. Sarabandi, "Ultrawideband characterization of complex dielectric constant of planar materials for 5G applications," *IEEE Trans. Instrum. Meas.*, vol. 70, 2021, Art. no. 6009911.
- [22] "Eastman Butvar—B-79." Accessed: Apr. 6, 2022. [Online]. Available: <https://www.eastman.com/Pages/ProductHome.aspx?product=71095420>



Michigan in 2018. His research interests include passive microwave circuits, antennas, and electromagnetic materials characterization.

ABDELHAMID M. H. NASR (Graduate Student Member, IEEE) received the B.Sc. and M.Sc. degrees in electrical engineering from Ain-Shams University, Cairo, Egypt, in 2014 and 2018, respectively. He is currently pursuing the Ph.D. degree in electrical engineering from The University of Michigan at Ann Arbor, Ann Arbor, MI, USA. He was a Research and a Teaching Assistant with the Faculty of Engineering, Ain Shams University from 2014 to 2018. He joined the Radiation Laboratory with the University of



KAMAL SARABANDI (Life Fellow, IEEE) received the B.S. degree in electrical engineering from the Sharif University of Technology, Tehran, Iran, in 1980, and the first M.S. degree in electrical engineering, the second M.S. degree in mathematics, and the Ph.D. degree in electrical engineering from The University of Michigan at Ann Arbor in 1986 and 1989, respectively.

He is currently the Director of the Radiation Laboratory and the Rufus S. Teesdale Endowed Professor of Engineering with the Department of

Electrical Engineering and Computer Science, The University of Michigan at Ann Arbor. He led the Center for Microelectronics and Sensors sponsored by the Army Research Laboratory under the Micro-Autonomous Systems and Technology Collaborative Technology Alliance Program from 2008 to 2018. He is currently leading a newly established center in Microwave Sensor Technology. He has published many book chapters and more than 280 papers in refereed journals on miniaturized and on-chip antennas, meta-materials, electromagnetic scattering, wireless channel modeling, random media modeling, microwave measurement techniques, radar calibration, inverse scattering problems, and microwave sensors. He has also had more than 650 papers and invited presentations in many national and international conferences and symposia on similar subjects. His research areas of interest include microwave and millimeter-wave radar remote sensing, meta-materials, electromagnetic wave propagation, and antenna miniaturization. Dr. Sarabandi served as a member of NASA Advisory Council appointed by the NASA Administrator for two consecutive terms from 2006 to 2010. He served as the President of the IEEE Geoscience and Remote Sensing Society (GRSS) in 2015 and 2016. He was a member of the Editorial Board of the *Proceedings of the IEEE* and an Associate Editor of the *IEEE TRANSACTIONS ON ANTENNAS AND PROPAGATION* and the *IEEE SENSORS JOURNAL*. He is a member of Commissions F and B of URSI and is serving as the Chair of the USNC URSI Commission F. He was a recipient of the Henry Russel Award from the Regent of The University of Michigan in 1997. In 1999, he received the GAAC Distinguished Lecturer Award from the German Federal Ministry for Education, Science, and Technology. He was also a recipient of the 1996 EECS Department Teaching Excellence Award. In 2005, he received the IEEE GRSS Distinguished Achievement Award and the University of Michigan Faculty Recognition Award. He was a recipient of the best paper Award at the 2006 Army Science Conference and the IEEE GRSS Symposium Best Paper Award in 2008 and 2017. In 2008, he was awarded a Humboldt Research Award from The Alexander von Humboldt Foundation of Germany. He was also awarded the 2010 Distinguished Faculty Achievement Award from the University of Michigan. The IEEE Board of Directors announced him the recipient of the 2011 IEEE Judith A. Resnik Award. He was recognized by the IEEE GRSS with its 2013 Education Award. He received a College of Engineering Research Excellence Award in 2004, the Stephen S. Attwood Award in 2017, and the Ted Kennedy Family Faculty Team Excellence Award in 2018 from the College of Engineering at the University of Michigan. In 2016, he was recognized as one of the top 50 Graduates of Sharif University of Technology. He also received a NASA Group Achievement Award for his contributions to NASA SMAP mission. In the past several years, joint papers presented by his students at a number of international symposia (IEEE APS'95,'97,'00,'01,'03,'05,'06,'07,'16 IEEE IGARSS'99,'02,'07,'11,'14, IEEE IMS'01, USNC URSI'04,'05,'06,'10,'11, AMTA '06, URSI GA '08,'14; Eastern Snow Conference '16) have received best paper awards.